Computers, Materials & Continua

Tech Science Press

https://doi.org/10.32604/cmc.2026.083127

ARTICLE

DFT-Based Computational Investigation of Mechanical, Acoustic and Thermal Properties of Cd1-xZnxTe Alloys for Radiation Detector Applications

Samir Dahmane[1], Mohammed Hadj Meliani[1], Mohamed Belabbas[2], Ismail Ouadha[3], Mohammed Traiche[1] and Noureddine Bouteldja[1,*]

[1]Laboratoire de Physique Théorique et de Physique des Matériaux (LPTPM), Faculty of Exact Sciences and Informatics, Hassiba Benbouali University of Chlef, Chlef, Algeria
[2]Department of Physics, Faculty of Exact Sciences and Informatics, Hassiba Benbouali University of Chlef, Chlef, Algeria
[3]Magnetic Materials Laboratory, Djillali Liabes University, Sidi Bel-Abbes, Algeria

*Corresponding Author: Noureddine Bouteldja. Email: n.bouteldja@univ-chlef.dz

Received: 30 March 2026; Accepted: 10 June 2026; Published: 23 July 2026

ABSTRACT: Zinc substitution in $Cd_{1-x}Zn_xTe$ (CZT) alloys emerges as a powerful strategy for engineering their structural, elastic, mechanical, acoustic and thermal properties, thereby enhancing their potential for high-performance optoelectronic and radiation detection applications. In this work, a comprehensive first-principles investigation based on Density Functional Theory, within both the Generalized Gradient Approximation and the Local Density Approximation, is conducted to systematically explore the composition-dependent behavior of CZT across the full concentration range ($0 \leq \times \leq 1$) in the cubic zinc-blende phase. The calculated elastic constants satisfy the Born stability criteria for all compositions, confirming the intrinsic mechanical stability of the alloys upon Zn incorporation. A pronounced and continuous increase in the bulk modulus, shear modulus and Young modulus is observed with increasing Zn content, revealing a significant enhancement in lattice rigidity driven by the formation of shorter, stronger Zn–Te bonds and improved bond covalency. Despite this stiffening, CZT alloys consistently exhibit ductile behavior, as demonstrated by positive Cauchy pressures, Pugh ratios well above the critical value for ductility ($B/G > 1.75$), and Poisson ratios within the range of 0.29–0.37, indicating a favorable balance between strength and deformability. The Vickers hardness shows a systematic increase from 1.89 to 6.66 GPa with Zn concentration, highlighting improved resistance to plastic deformation while maintaining the moderate hardness typical of II–VI semiconductors. Additionally, the moderate elastic anisotropy indicates controlled directional dependence without compromising structural integrity. Concurrently, the monotonic enhancement of the longitudinal, transverse and average sound velocities reflects increasingly efficient elastic wave propagation and improved lattice cohesion. The Debye temperature rises significantly from approximately 163 to 227 K, providing strong evidence of reinforced interatomic bonding and superior thermal stability. Collectively, these results deliver a coherent and in-depth theoretical framework demonstrating that the physical properties of CZT alloys can be precisely tuned through compositional engineering. This tunability, combined with their inherent stability and balanced mechanical performance, positions CZT as a highly promising and versatile material platform. It is well suited for next-generation radiation detectors and advanced semiconductor devices operating, even under demanding mechanical and thermal conditions.

KEYWORDS: DFT; CZT; rigidity; ductility; elasticity; mechanical stability; sound velocity; thermal stability

1 Introduction

II–VI semiconductor compounds and their alloys have been extensively studied due to their remarkable physical, optical and structural properties. These characteristics make them highly relevant for modern electronic and optoelectronic applications [1–3]. Among these materials, Cadmium Zinc Telluride (CdZnTe, CZT) has attracted significant attention because of its tunable properties and broad technological applications. Crystallizing in the B3 zinc-blende structure under ambient conditions, CZT serves as a key material for room-temperature radiation detectors, photovoltaic devices and electro-optic modulators [4,5]. Its principal advantage lies in the ability to continuously adjust both the band gap and lattice parameter through Zn concentration. This tunability enables precise tailoring of material characteristics for specific device requirements [6].

The binary end members, CdTe and ZnTe, are direct band-gap semiconductors with energy gaps of approximately 1.48 and 2.22 eV, respectively [7]. CdTe is widely utilized in thin-film photovoltaic technology owing to its near-ideal band gap for solar energy conversion and high optical absorption coefficient [8]. ZnTe is commonly used as a p-type back contact layer in CdTe-based solar cells, because of its suitable band alignment and ability to reduce the Schottky barrier at the back interface. This improves hole transport and overall device efficiency [9]. Recent advances in nanostructured CdTe/ZnTe core/shell systems have demonstrated enhanced charge carrier mobility, and improved photo-electrode performance for solar cell applications [10].

Alloying CdTe and ZnTe produces a continuous solid solution across the full composition range. This generally follows Vegard law, with minor deviations characterized by the bowing parameter [11]. Substituting Cd with the smaller Zn atom systematically influences structural, elastic, acoustic and thermal properties. These properties are essential in determining device performance [12].

CZT alloys are particularly advantageous for radiation detection due to their high effective atomic number (Z_{eff} = 50). This ensures efficient absorption of high-energy photons. Their wide band gap minimizes leakage current, allowing room-temperature operation without cryogenic cooling [13,14]. Recent studies have demonstrated that large-volume CZT detectors (4 cm^3) exhibit excellent energy resolution, and efficiency for underwater γ-radiation sensing applications. Aluminum housing has been identified as optimal for marine deployment [15]. Consequently, CZT detectors are widely applied in medical imaging systems, such as Single Photon Emission Computed Tomography (SPECT) and Positron Emission Tomography (PET), as well as in security and nuclear monitoring [16,17].

The physical properties of CZT, including band gap and lattice constant, are strongly composition-dependent. Increasing Zn content gradually widens the band gap and nearly linearly reduces the lattice parameter. This tunability enables control of strain in heterostructures, facilitates epitaxial growth on diverse substrates, and makes CZT an ideal candidate for advanced optoelectronic and radiation-detection devices [18].

Several theoretical and experimental studies have examined the fundamental electronic and optical properties of $Cd_{1-x}Zn_xTe$ alloys. Wei et al. [19] employed first-principles calculations to explain band gap bowing, showing that the valence band maximum is mainly Te p-states and the conduction band minimum cation s-states. Sher et al. [20] highlighted the role of chemical bonding in determining alloy electronic structure. Recent first-principles investigations using HSE and mBJ functionals have demonstrated the significant impact of atomic disorder on band gap energy, and thermodynamic stability across the full composition range. They also revealed distinct behavior under biaxial strain in different crystal planes [21]. Barone et al. [22] investigated $Zn_xCd_{1-x}Te$ superlattices, demonstrating that stacking order can alter the band

gap by ~0.2 eV. Dumre et al. [23] showed that short-range order significantly impacts phase equilibria and optoelectronic properties of $Zn_xCd_{1-x}Te$ alloys.

Optical behavior has been explored extensively. Sharma et al. [24] reviewed CdZnTe thin films as absorber layers for photovoltaic applications. Experimental studies of annealed films produced by electrodeposition showed band gaps tunable between 1.72 and 2.22 eV depending on annealing temperature, with improved surface morphology and grain structure for solar cells [25]. Tedjini et al. [26] investigated the electronic structure and optical properties of $Cd_{1-x}Zn_xTe$ using TB-mBJ first-principles calculations, providing insight into the effect of Zn incorporation on the material fundamental characteristics.

Transport properties, including electrical conductivity, Hall effect, carrier mobility and thermoelectric power, have also been extensively studied in CZT crystals. These studies reveal typical semiconducting behavior along with high resistivity values (10^9–10^{10} Ω·cm), which are essential for reducing leakage currents in radiation detector applications [27]. Recent characterization of CZT detectors for broadband applications has confirmed resistivity of approximately 1.9×10^{10} Ω·cm, and energy resolution of 4.3% with ^{137}Cs sources, demonstrating linear response across diagnostic X-ray and therapeutic radiation beams [28].

CZT alloys also exhibit interesting defect, magnetic and vibrational behaviors. Microscopic defects in Al-doped CZT, such as Al_Cd^+ donors and V_Cd–Al_Cd acceptor complexes, significantly influence charge transport and carrier lifetimes [29]. While pure CZT is non-magnetic, doping with transition metals like Mn or Cr can induce half-metallic behavior with complete spin polarization [30]. Vibrational properties, including longitudinal optical (LO) and transverse optical (TO) phonon frequencies, exhibit one-mode behavior with composition. This provides insight into lattice dynamics and disorder through Raman spectroscopy [31]. Recent time-resolved photoluminescence studies on self-assembled CdZnTe quantum dots by M.T. Man and H.S. Lee have revealed thermally activated transitions, with localization energies of approximately 8 meV. These studies demonstrate that quantum confinement influences both exciton–acoustic phonon and exciton–LO phonon interactions, with multi-phonon absorption processes involving LO phonons near 19.2 meV, contributing to carrier dynamics [32,33].

Formation of defects, including Cd-vacancies, Te-antisites and Te-inclusions, leads to deterioration in charge collection efficiency due to carrier trapping [34]. Advanced three-dimensional position resolution and energy spectrum calibration techniques, using finite element and Monte Carlo methods, have been developed to mitigate signal response distortion in the near-anode region, enabling improved energy resolution and effective sensitive volume in pixelated CZT detectors [35].

Exchange and correlation interactions substantially affect the electronic and transport properties of semiconductors. Exchange interactions reflect the tendency of electrons to align spins, while correlation interactions describe electron-electron influences, impacting electronic structure and transport [36,37]. In density functional theory calculations, the choice of exchange-correlation functional significantly affects predicted properties. The local density approximation (LDA) tends to overbind atoms, resulting in smaller equilibrium volumes and stiffer elastic responses [38], whereas the generalized gradient approximation (GGA) typically corrects this overbinding but may overestimate lattice constants [39,40].

$Cd_{1-x}Zn_xTe$ alloys have attracted considerable attention owing to their remarkable potential in optoelectronic devices and room-temperature radiation detectors, where mechanical reliability and lattice stability are essential for long-term device performance. In the present work, a comprehensive first-principles study is carried out to investigate the influence of Zn incorporation on the structural, elastic, mechanical, acoustic and thermal properties of CZT alloys over the entire compositional range ($0 \leq \times \leq 1$). Particular emphasis is placed on understanding how progressive Zn substitution modifies lattice rigidity, elastic resistance, ductility, anisotropic behavior, sound-wave propagation and Debye temperature. Special attention is devoted

to the intermediate compositions, which remain comparatively less explored despite their technological importance for compositional engineering and performance optimization. To ensure the robustness and reliability of the predicted properties, calculations were performed using both the LDA and GGA, allowing a systematic evaluation of functional-dependent variations. The combined analysis of elastic constants, mechanical moduli, acoustic velocities and thermic indicators provides deeper insight into the relationship between alloy composition, bonding characteristics and lattice dynamics, thereby establishing a reliable theoretical framework, for the design and optimization of CZT-based materials in advanced optoelectronic and radiation-detection applications.

2 Method of Calculations

To investigate the structural, elastic, mechanical, acoustic and thermal properties of $Cd_{1-x}Zn_xTe$ alloys, we performed first-principles calculations based on Density Functional Theory (DFT) [41,42]. All computations were carried out using the WIEN2k package, which implements the Full Potential Linearized Augmented Plane Wave (FP-LAPW) method [43–45]. This approach is widely recognized for its accuracy in describing the electronic and physical properties of crystalline solids, as it makes no shape approximations for the potential or charge density in the interstitial region. To evaluate the influence of the exchange-correlation functional on our predictions, we employed both the LDA and the GGA as parameterized by Perdew, Burke and Ernzerhof (PBE) [46,47]. This dual approach allows for a systematic comparison and helps identify trends that are robust against the specific choice of functional.

The unit cell is divided into non-overlapping Muffin-Tin (MT) spheres centered on the atoms and an Interstitial Region (IR). Inside the MT spheres, the wave functions, charge density and potential are expanded in spherical harmonics, while plane waves are used in the IR. The MT radii were chosen as 2.5 a.u. for Cd, 2.3 a.u. for Zn and 2.4 a.u. for Te to ensure convergence and avoid sphere overlap. The plane-wave cutoff parameter was set to $R_{MT} \times K_{max} = 8.0$, a value commonly adopted for II–VI semiconductors to ensure a well-converged basis set. The maximum angular momentum inside the MT spheres was $l_{max} = 10$ and the charge density was expanded up to $G_{max} = 12$ (a.u.)$^{-1}$. Core and valence states were separated by an energy cutoff of −6.0 Ry. Brillouin zone integrations were performed using 1000 k-points to ensure accurate sampling and convergence of the total energy, as confirmed by preliminary tests. Self-consistent calculations were continued until the total energy converged to 10^{-5} Ry.

The CZT alloy crystallizes in the cubic zinc-blende (B3) structure (space group F-43m, No. 216), where the cation sites at (0, 0, 0) are shared by Cd and Zn atoms, while the anion site at (1/4, 1/4, 1/4) is occupied by Te atom, forming a tetrahedral coordination. To model the alloy at specific compositions (x = 0.25, 0.5 and 0.75), structures were constructed using a (1 × 1 × 1) conventional zinc-blende unit cell containing 8 atoms (4 cation atoms and 4 anion atoms). Cd and Zn atoms were distributed over the cation sublattice according to the desired stoichiometry, while Te atoms fully occupied the anion sublattice. All structures, including the binary endpoints (x = 0 and x = 1), were fully relaxed to ensure structural stability, preserve the tetrahedral bonding environment and accurately capture the composition-dependent evolution of the material properties. The distribution of atomic positions is summarized in Table 1 and illustrated in Fig. 1.

Table 1: Atomic positions of $Cd_{1-x}Zn_xTe$ alloys in the zinc-blende structure.

	Cd	Zn	Te
Electronics configuration	[Kr] $4d^{10}5s^2$	[Ar] $3d^{10}4s^2$	[Kr] $4d^{10}5s^25p^4$
CdTe	(0, 0, 0)	/	(¼, ¼, ¼)
$Cd_{0.75}Zn_{0.25}Te$	(0, 0, 0) (½, ½, 0) (½, 0, ½)	(0, ½, ½)	(¼, ¼, ¼) (¾, ¾, ¼) (¾, ¼, ¾) (¼, ¾, ¾)
$Cd_{0.50}Zn_{0.50}Te$	(0, 0, 0) (½, ½, 0)	(½, 0, ½) (0, ½, ½)	
$Cd_{0.25}Zn_{0.75}Te$	(0, 0, 0)	(½, ½, 0) (½, 0, ½) (0, ½, ½)	
ZnTe	/	(0, 0, 0)	(¼, ¼, ¼)

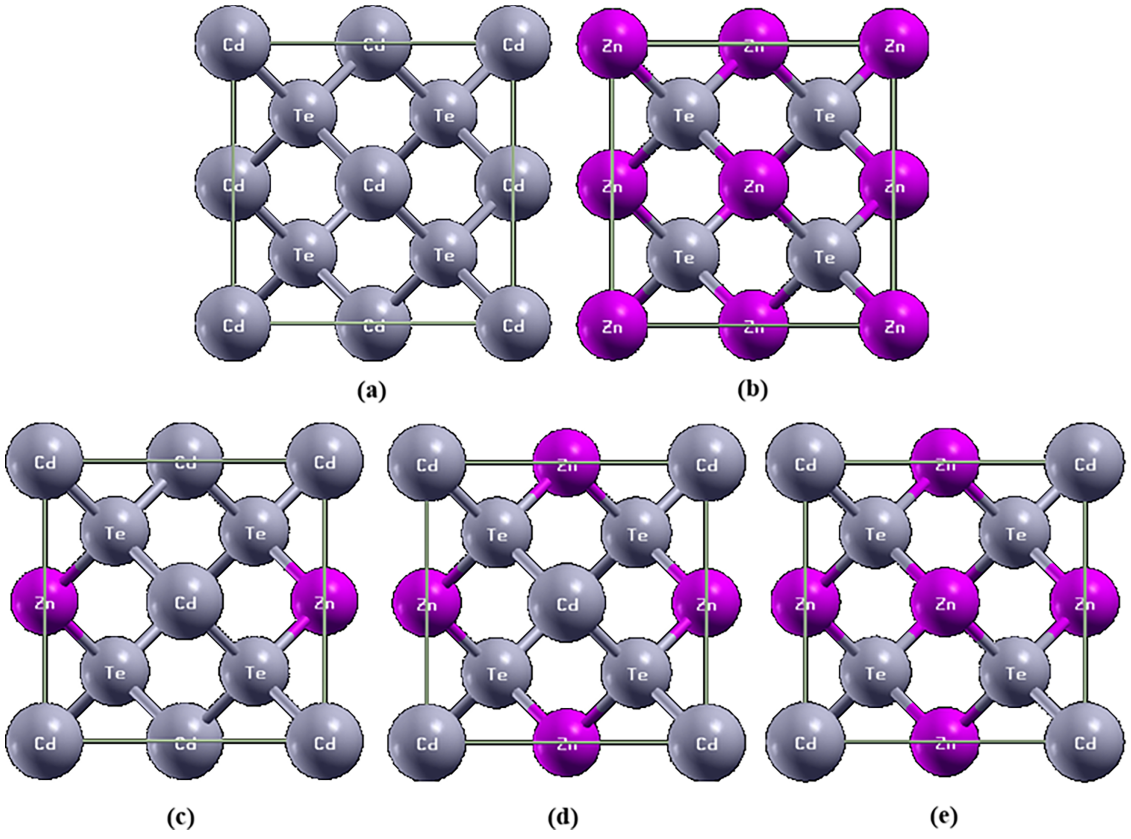

Figure 1: Zinc-blende structure of binary (**a**) CdTe and (**b**) ZnTe, and their ternary $Cd_{1-x}Zn_xTe$ supercells for (**c**) x = 0.25, (**d**) x = 0.50, and (**e**) x = 0.75.

3 Results and Discussion

3.1 Equilibrium Properties

To determine the ground-state equilibrium properties of $Cd_{1-x}Zn_xTe$ alloys in the zinc-blende structure, full structural relaxation was first performed to obtain the minimum total energy configuration for each composition (x = 0, 0.25, 0.5, 0.75 and 1.0). The equilibrium lattice constant *a* was then determined by calculating the total energy as a function of unit-cell volume using the 2D-optimize package [48]. The obtained energy–volume data were fitted using the Birch–Murnaghan equation of state [49]. The calculated lattice parameters within both LDA and GGA approximations are presented in Table 2.

Table 2: Equilibrium lattice constant for $Cd_{1-x}Zn_xTe$ zinc-blende at various compositions x.

		Composition (x%)				
	Method	**0**	**25**	**50**	**75**	**100**
Lattice constant a (Å)	**FP-LPAW LDA**	6.42	6.35	6.25	6.14	6.01
	FP-LPAW GGA	6.64	6.53	6.44	6.32	6.21
	Exp	6.482 [50]				6.105 [51]
	Others	6.422 [12]		6.135 [12]		5.983 [12]
		6.456 [52]		6.433 [52]		6.077 [52]
		6.40 [53]		6.415 [52]		6.1026 [54]

As shown in Fig. 2, the lattice constant of $Cd_{1-x}Zn_xTe$ decreases monotonically with increasing Zn content, from 6.42–6.64 Å for CdTe to 6.01–6.21 Å for ZnTe, in excellent agreement with Vegard law [11]. This systematic contraction arises directly from the smaller atomic radius of Zn (1.34 Å) compared to Cd (1.48 Å), which shortens the average bond length and enhances orbital overlap as Zn concentration increases. The GGA functional consistently yields larger lattice constants than LDA across all compositions, a well-established behavior where LDA underestimates due to its overbinding character, while GGA slightly overestimates via gradient corrections. Notably, the discrepancy between the two functionals diminishes at higher Zn concentrations, reflecting reduced sensitivity to the exchange-correlation treatment as the lattice becomes dominated by the stiffer Zn–Te bonding network. The calculated values show excellent agreement with available experimental measurements and previous theoretical studies, validating the accuracy of the present computational methodology. This composition-driven lattice contraction underpins the subsequent enhancement of elastic stiffness, mechanical strength, and thermal stability detailed in the following sections.

3.2 Elastic Properties

The elastic constants were evaluated on the basis of Hooke Law, which establishes a linear relationship between the applied stress and the resulting strain in the elastic regime [55]. In tensor notation, the relation between the elastic constants C_{ijkl}, the strain tensor ε_{kl} and the stress tensor σ_{ij} can be expressed as:

$$C_{ijkl} = \frac{\sigma_{ij}}{\varepsilon_{kl}}, \tag{1}$$

To determine the elastic constants of $Cd_{1-x}Zn_xTe$ alloys at their optimized lattice constants, the calculations were performed using the Hex-elastic computational package [56]. Within this approach, the elastic stiffness constants were obtained by applying small, symmetry-adapted strains to the equilibrium structure, and extracting the second derivative of the total energy with respect to strain:

$$C_{ij} = \frac{1}{V_0}\frac{\partial^2 E}{\partial\varepsilon_i \partial\varepsilon_j}, \tag{2}$$

where V_0 the equilibrium volume, E the total energy and ε the applied infinitesimal lattice strain. This energy–strain approach yields elastic parameters from the curvature of the energy surface at equilibrium.

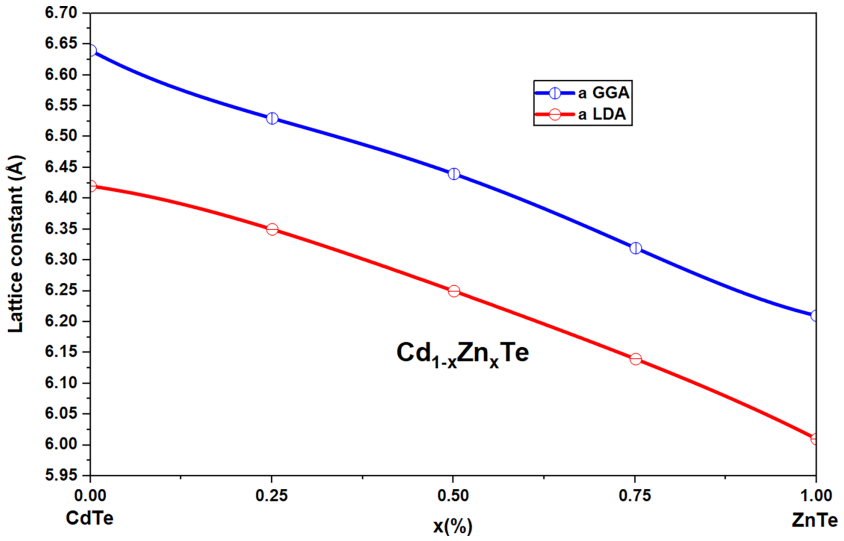

Figure 2: Equilibrium lattice constant of $Cd_{1-x}Zn_xTe$ as a function of Zn concentration (**x**).

All elastic constants were calculated within the DFT framework using GGA and LDA exchange–correlation potentials for different Zn compositions, as summarized in Table 3.

Table 3: Elastic constants for $Cd_{1-x}Zn_xTe$ zinc-blende at various compositions x.

		Composition x (%)				
	Method	**0**	**25**	**50**	**75**	**100**
C_{11}(GPa)	**FP-LAPW LDA**	59.25	67.43	77.81	82.76	78.98
	FP-LAPW GGA	57.61	66.39	73.71	80.65	78.29
	Exp	53.5 [57]				72.2 [58]
	Others	62.3 [51]		79.93 [12]		78.63 [12]
		57.3 [59]		74.50 [12]		82 [60]
C_{12}(GPa)	**FP-LAPW LDA**	41.63	43.41	45.87	48.03	44.70
	FP-LAPW GGA	39.60	42.48	45.27	45.43	42.36
	Exp	36.81 [57]				40.9 [58]
	Others	27 [51]		44.06 [12]		43.72 [12]
		39.63 [60]		44.99 [12]		42 [60]
C_{44}(GPa)	**FP-LAPW LDA**	23.02	27.22	31.32	36.91	40.23
	FP-LAPW GGA	19.98	26.71	30.12	36.27	38.41
	Exp	19.9 [57]				30.8 [58]
	Others	25.1 [51]		36.11 [12]		35.61 [12]
		19.04 [60]		32.63 [12]		55 [60]

Fig. 3 shows the composition-dependent elastic constants C_{11}, C_{12} and C_{44} of $Cd_{1-x}Zn_xTe$ alloys calculated using LDA and GGA. All constants increase monotonically with Zn content, reflecting lattice stiffening due to the substitution of Cd with smaller Zn atoms and the formation of strongly bonded Zn–Te. Specifically, C_{11} rises from ~57–59 to 78–79 GPa, indicating enhanced longitudinal stiffness, while C_{12} increases moderately from 39–42 to 42–45 GPa, reflecting gradual strengthening of transverse deformation resistance. In contrast, C_{44} shows the largest enhancement, nearly doubling from 20–23 to 38–40 GPa, highlighting improved shear resistance. All values satisfy the Born stability criteria for cubic crystals ($C_{11} > 0$, $C_{44} > 0$, $C_{11} - C_{12} > 0$, $C_{11} + 2C_{12} > 0$) [61], thereby confirming mechanical stability across the composition range. LDA predicts slightly higher values than GGA due to its overbinding tendency, although both functionals exhibit consistent qualitative trends. Collectively, these results demonstrate that Zn incorporation systematically strengthens the lattice while preserving structural integrity.

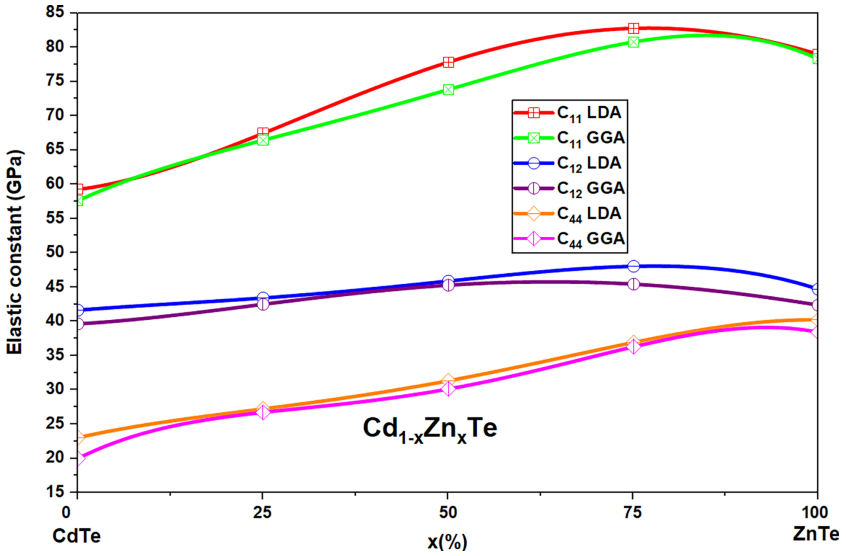

Figure 3: Composition dependence of the elastic constants for $Cd_{1-x}Zn_xTe$ alloys.

3.3 Mechanical Properties

The mechanical behavior of $Cd_{1-x}Zn_xTe$ alloys was further analyzed by calculating key polycrystalline elastic moduli, derived from the single-crystal elastic constants. Using the Voigt–Reuss–Hill (VRH) averaging scheme [62], the bulk modulus (B), shear modulus (G) and Young modulus (E) were determined, providing detailed insight into the stiffness and bonding characteristics of the alloy system. In addition, the Pugh ratio (B/G), Poisson ratio (ν) and Cauchy pressure (P_C) were computed to assess the ductile or brittle nature of the materials. The elastic anisotropy factor (A) was evaluated to quantify the directional variation of the elastic response. Furthermore, the Vickers hardness (H_V) was also estimated to evaluate the resistance of the alloys to plastic deformation. The complete set of calculated mechanical properties for various Zn concentrations within both LDA and GGA approximations are summarized in Table 4.

3.3.1 Bulk Modulus

The bulk modulus (B) is a fundamental mechanical parameter that quantifies a material resistance to uniform compression, providing vital insight into its structural stiffness and response to external pressure. In cubic crystals, the bulk modulus can be accurately determined from the single-crystal elastic constants, capturing how the lattice resists volume changes under hydrostatic stress. This relationship bridges the

microscopic elastic behavior of the crystal with its macroscopic mechanical properties, allowing predictions of material performance under various mechanical and operational conditions. The bulk modulus for cubic systems is calculated using the expression [63]:

$$B = \frac{C_{11} + 2C_{12}}{3} \tag{3}$$

Table 4: Bulk modulus (B), Shear modulus (G), Young modulus (E), Cauchy pressure (P_C), Pugh ratio (B/G), Vickers hardness (H_V), Poisson ratio (ν) and Anisotropy factor (A) for $Cd_{1-x}Zn_xTe$ zinc-blende at various compositions x.

x(%)	Method	B (GPa)	G (GPa)	E (GPa)	P_C (GPa)	H_V (GPa)	B/G	ν	A
0	FP-LAPW LDA	47.50	15.67	42.73	18.61	2.23	3.03	0.36	2.61
	FP-LAPW GGA	45.62	14.50	39.80	19.65	1.89	3.15	0.37	2.22
	Others	46.68 [64]	19.89 [65]	41.45 [65]		3.081 [65]		0.338 [65]	
		42.75 [65]		49.55 [66]				0.33 [67]	
		46.18 [67]							
25	FP-LAPW LDA	51.42	19.60	53.45	16.19	3.49	2.62	0.35	2.20
	FP-LAPW GGA	50.46	19.36	52.40	15.77	3.46	2.61	0.35	2.23
50	FP-LAPW LDA	56.52	23.90	63.65	14.55	4.74	2.36	0.34	1.96
	FP-LAPW GGA	54.75	22.31	60.45	15.15	4.27	2.45	0.35	2.11
75	FP-LAPW LDA	59.61	27.27	72.96	11.12	5.75	2.19	0.34	2.13
	FP-LAPW GGA	57.17	27.18	72.63	9.16	5.94	2.11	0.33	2.05
100	FP-LAPW LDA	56.13	28.57	74.08	4.47	6.58	1.97	0.30	2.35
	FP-LAPW GGA	54.34	28.31	73.26	3.96	6.66	1.92	0.29	2.14
	Others	55.67 [64]		64.42 [68]		4 [69]		0.276 [68]	3.86 [68]
		51.23 [68]							

As shown in Fig. 4a, the bulk modulus of $Cd_{1-x}Zn_xTe$ alloys exhibits a steady increase with increasing Zn content. Specifically, B rises from approximately 45–47 GPa for CdTe to 54–56 GPa for ZnTe, reflecting an enhancement of resistance to compressibility under hydrostatic pressure. This behavior originates from the substitution of longer Cd–Te bonds by shorter Zn–Te bonds, which leads to a denser and more energetically rigid lattice. Across all compositions, LDA consistently predicts higher bulk moduli than GGA, due to its tendency to overestimate interatomic binding strength and reduce equilibrium volume. The compositional dependence of B shows a near-linear rise up to x = 0.75, followed by slight saturation or minor reduction at x = 1.0, suggesting that the alloy approaches the intrinsic compressional limit of the ZnTe.

3.3.2 Shear Modulus

The shear modulus *G*, which describes resistance to shape deformation without volume change, was calculated using the Hill average of the Voigt and Reuss bounds [62]:

$$G = \frac{G_V + G_R}{2}, \tag{4}$$

where:

$$G_V = \frac{C_{11} - C_{12} + 3C_{44}}{5}, \tag{5}$$

$$G_R = \frac{5(C_{11} - C_{12})C_{44}}{4C_{44} + 3(C_{11} - C_{12})}, \tag{6}$$

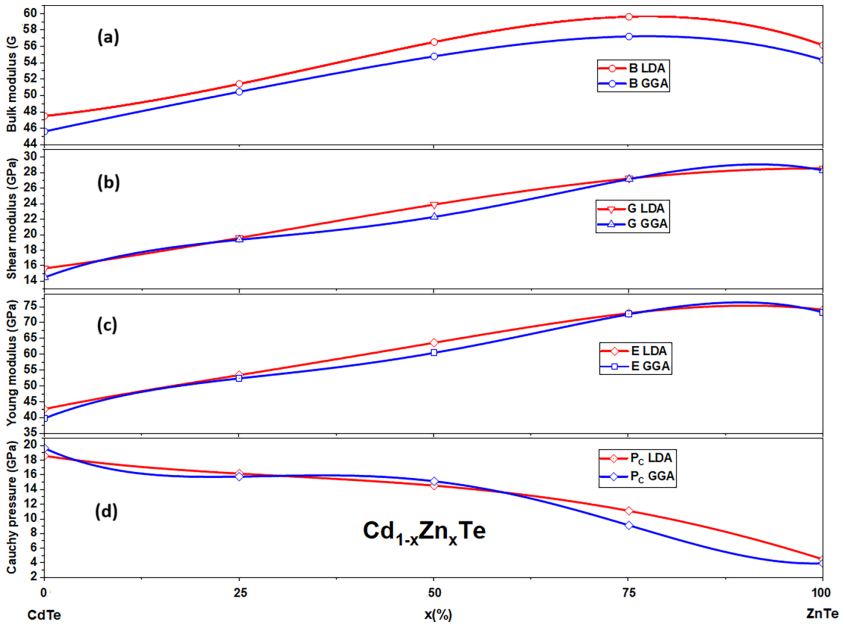

Figure 4: Mechanical properties of $Cd_{1-x}Zn_xTe$ as a function of Zn concentration: (**a**) Bulk modulus B; (**b**) Shear modulus G; (**c**) Young modulus E; (**d**) Cauchy pressure P_C.

As illustrated in Fig. 4b, the shear modulus, which measures the material resistance to lattice distortion, increases markedly with rising Zn content. Specifically, G rises from approximately 14–15 GPa for CdTe to 28–29 GPa for ZnTe, indicating a significant enhancement in the alloy ability to resist non-uniform deformation and shape change. This enhancement is associated with the increasing role of directional bonding constraints within the alloyed lattice, which strengthens resistance against shear strain. The difference between LDA and GGA predictions becomes more pronounced at higher Zn concentrations, emphasizing the sensitivity of shear response to exchange–correlation treatment of anisotropic bonding interactions.

3.3.3 Young Modulus

The Young modulus *E*, which measures stiffness under uniaxial stress, was derived from *B* and *G* using [70]:

$$E = \frac{9BG}{3B + G}, \tag{7}$$

As depicted in Fig. 4c, Young modulus, which quantifies tensile rigidity, exhibits a trend similar to those of the bulk and shear moduli. E increases from approximately 39–42 GPa for CdTe to 73–74 GPa for ZnTe, showing a nearly linear rise up to x = 0.75, followed by a plateau at higher Zn concentrations. This trend confirms that Zn incorporation progressively enhances uniaxial stiffness by reinforcing the combined volumetric and shear resistance of the lattice. The saturation behavior suggests that beyond intermediate compositions, the alloy approaches a regime where further substitution yields limited additional strengthening of the elastic framework. The LDA functional predicts higher values than GGA due to its stronger binding-driven stiffening of interatomic interactions.

3.3.4 Cauchy Pressure

The Cauchy pressure is an important parameter for evaluating the nature of atomic bonding in materials, defined as [71]:

$$P_C = C_{12} - C_{44}, \tag{8}$$

As shown in Fig. 4d, the Cauchy pressure remains positive across the entire composition range, varying from approximately 4 to 20 GPa. This behavior strongly indicates ductile mechanical response dominated by central-force interactions. as positive Cauchy pressures are typically associated with central-force-dominated bonding and metallic-like behavior, whereas negative values reflect directional covalent bonding and brittleness. The slight decrease in P_C with increasing Zn content suggests a gradual shift toward greater angular (directional) bonding contributions, consistent with the evolution observed in the shear modulus. Thus, Cauchy pressure serves as a direct indicator of the balance between metallic-like central forces and covalent directional bonding character. The slightly higher values predicted by GGA compared to LDA reflect its tendency to favor a more delocalized, and less overbound electronic structure.

3.3.5 Vickers Hardness

The Vickers hardness (H_V), a widely used indicator of a material resistance to localized plastic deformation, can be estimated from the bulk modulus (B) and shear modulus (G) using the empirical correlation proposed by Chen et al. [72]. This formulation, expressed as:

$$H_V = 2\left(\frac{G^2}{B}\right)^{0.585} - 3, \tag{9}$$

Fig. 5a provides insight into the Vickers hardness of $Cd_{1-x}Zn_xTe$ alloys as a function of composition. The hardness exhibits a pronounced monotonic increase with Zn content, rising from approximately 1.89–2.23 GPa for CdTe to 6.58–6.66 GPa for ZnTe. This enhancement reflects a progressive strengthening of the elastic framework, consistent with reduced bond length and increased resistance to plastic deformation. The increase in hardness correlates directly with the simultaneous rise in the shear modulus (G) and the G^2/B ratio, confirming the consistency of hardness with shear-driven mechanical resistance. At intermediate compositions (x = 0.50 and 0.75), H_V exceeds 4.27 GPa, indicating a transition toward a mechanically robust regime suitable for device applications. Minor differences between LDA and GGA are noticeable at Cd-rich compositions but diminish toward ZnTe, indicating that compositional strengthening dominates over functional dependence in the high-Zn limit.

3.3.6 Pugh Ratio

The Pugh ratio (B/G) was employed to assess the ductile or brittle nature of $Cd_{1-x}Zn_xTe$ (CZT) alloys. According to the Pugh criterion, materials with B/G > 1.75 are considered ductile, whereas lower values indicate brittleness [73,74].

Fig. 5b displays the compositional dependence of B/G across the studied alloys. The calculated ratios range from approximately 1.92 to 3.15, remaining well above the critical threshold and confirming that all compositions preserve ductile behavior. The B/G ratio gradually decreases with increasing Zn content, reflecting a systematic balance shift between volumetric and shear resistance, consistent with the stiffening observed in both bulk and shear moduli. At the CdTe-rich limit (x = 0), GGA yields a slightly higher B/G (3.15) than LDA (3.03), while at the ZnTe-rich end (x = 1), both functionals yield comparable values

(1.92–1.97), indicating that ductility becomes less sensitive to the exchange–correlation description as bonding stiffens. Overall, the trend links mechanical ductility directly to the evolving dominance of shear resistance over compressibility across the alloy series.

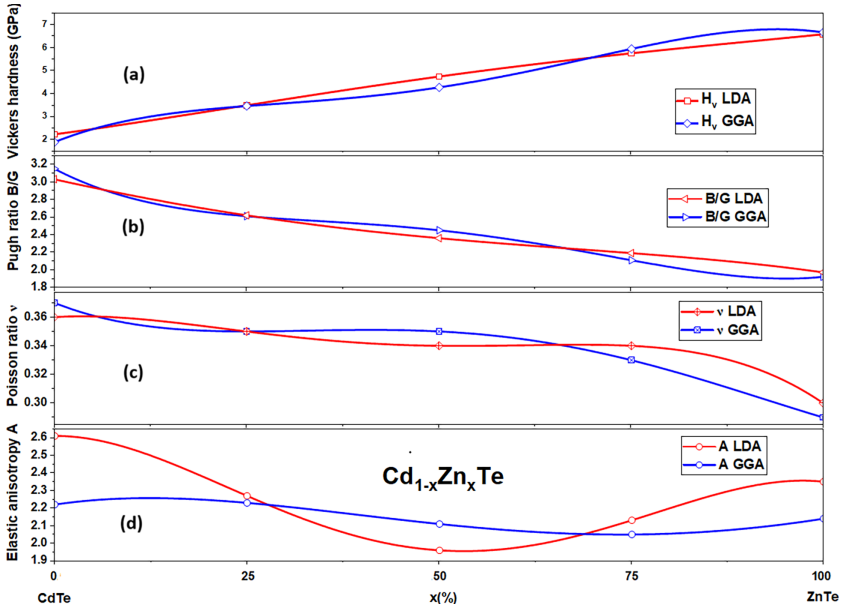

Figure 5: Derived mechanical indicators of $Cd_{1-x}Zn_xTe$ vs. Zn content: (**a**) Vickers hardness H_V; (**b**) Pugh ratio B/G; (**c**) Poisson ratio *v*; (**d**) Elastic anisotropy factor A.

3.3.7 Poisson Ratio

The Poisson ratio (v) provides information about the resistance of a material to shear deformation and the nature of interatomic bonding. It was calculated using the relation [75]:

$$\nu = \frac{3B - 2G}{2(3B + G)}, \tag{10}$$

As evident in Fig. 5c, the Poisson ratio provides complementary insight into bonding character and deformation behavior. Across all compositions. Across all compositions, v ranges from approximately 0.29 to 0.37, consistent with ductile, centrally dominated bonding interactions. Its gradual decrease with increasing Zn content, indicating a progressive reduction in lateral strain response as directional bonding strengthens. Small differences between LDA and GGA reflect subtle variations in predicted bond localization, but both converge at intermediate compositions, where compositional disorder moderates functional sensitivity. This convergence highlights that elastic response becomes increasingly, governed by alloying effects rather than methodological differences.

3.3.8 Elastic Anisotropy Factor

The elastic anisotropy factor (A) (Zener factor) describes the directional dependence of elastic properties in crystalline materials. It was calculated using the relation [76]:

$$A = \frac{2C_{44}}{C_{11} - C_{12}}, \tag{11}$$

As shown in Fig. 5d, The $Cd_{1-x}Zn_xTe$ system exhibits moderate elastic anisotropy across the full composition range, with the Zener factor A varying from 1.96 to 2.61. A clear non-monotonic behavior is observed, where A decreases from CdTe (A = 2.22–2.61) to a minimum at intermediate Zn concentrations (A = 1.96–2.11 at x = 0.50), followed by a slight increase toward ZnTe (A = 2.14–2.35). This trend reflects a partial compensation between the elastic constants C_{44} and $C_{11}-C_{12}$, governed by the competition between Cd–Te and stronger Zn–Te bonding interactions. As a result, the alloy exhibits reduced anisotropy at intermediate compositions, indicating a more balanced and homogeneous elastic response compared to the binary end members. In this regime, the more uniform distribution of elastic stiffness is particularly beneficial when the material is employed as a substrate in heterostructures, as it reduces strain energy accumulation at interfaces and enhances strain accommodation. Overall, compositions near x = 0.5 provide an optimal combination of structural robustness and near-isotropic elastic behavior, making them favorable for heterostructure-based device applications. The slight enhancement of anisotropy predicted within LDA reflects its intrinsic overbinding nature, which strengthens directional bonding contributions and increases the contrast between elastic constants, whereas GGA generally provides a more relaxed electronic description, and a comparatively reduced anisotropic response. Both functionals, however, tend to converge at intermediate compositions, suggesting that compositional disorder promotes an averaging effect that mitigates directional bonding disparities.

The three-dimensional surfaces shown in Fig. 6a–e illustrate the directional dependence of Young modulus E, for $Cd_{1-x}Zn_xTe$ alloys along the full composition range. For CdTe, the distribution of E exhibits a strongly distorted, non-spherical shape with pronounced lobes along specific crystallographic directions, indicating significant elastic anisotropy. This behavior reflects the directional nature of Cd–Te bonding and the unequal stiffness response along different crystal axes. As Zn content increases, the shape of the elastic surface gradually becomes more uniform, with reduced directional distortion and a smoother, more rounded topology. This transition indicates a progressive reduction in anisotropy and a more balanced distribution of elastic stiffness, arising from the increasing contribution of stronger and more homogeneous Zn–Te bonds. At intermediate compositions, particularly around x = 0.50, the surface approaches a more quasi-spherical form, suggesting an almost isotropic elastic response where directional dependence is minimized. However, as the composition approaches ZnTe, a slight re-emergence of directional features is observed, reflecting the intrinsic anisotropy of the ZnTe endpoint. Overall, the evolution from elongated, lobe-like surfaces (anisotropic behavior) toward more spherical geometries (isotropic behavior), clearly demonstrates that intermediate compositions exhibit the most mechanically uniform response, which is beneficial for reducing strain localization in device applications such as radiation detectors and heterostructure substrates.

3.4 Acoustic Properties

The acoustic behavior of $Cd_{1-x}Zn_xTe$ alloys is fundamentally governed by the compositional dependence of the longitudinal (v_l), transverse (v_t) and average (v_m) sound velocities. These velocities, derived rigorously from the elastic moduli via the Christoffel equation [77], constitute fundamental parameters governing elastic wave propagation. Beyond their descriptive utility, they serve as incisive probes of lattice dynamics, offering direct insight into the mechanical stiffness and the intrinsic bond strength that characterize the alloy system. The calculated sound velocities as a function of Zn concentration within both LDA and GGA approximations are compiled in Table 5.

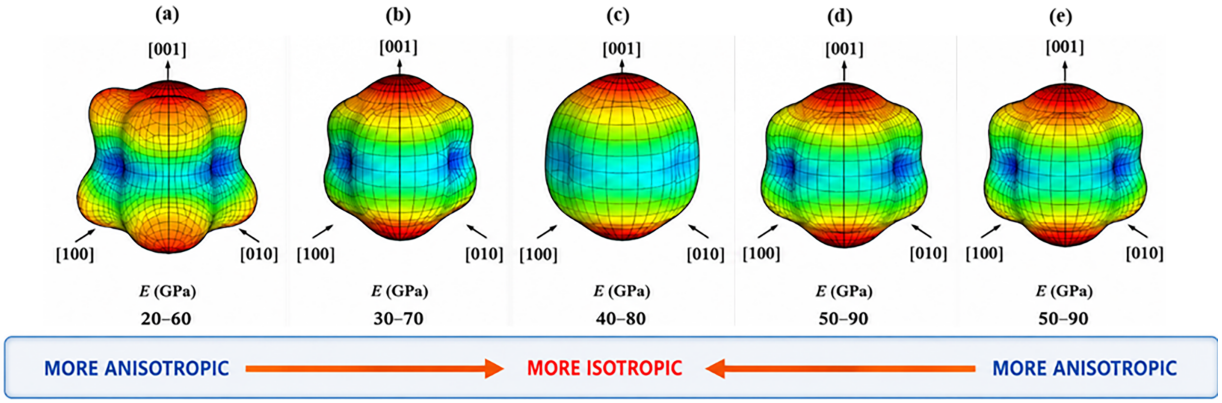

Figure 6: Three-Dimensional Young modulus surfaces showing the elastic anisotropy of $Cd_{1-x}Zn_xTe$ alloys: (**a**) CdTe, (**b**) $Cd_{0.75}Zn_{0.25}Te$, (**c**) $Cd_{0.50}Zn_{0.50}Te$, (**d**) $Cd_{0.25}Zn_{0.75}Te$ and (**e**) ZnTe.

Table 5: Longitudinal (v_l), transverse (v_t), average (v_m) sound velocities and Debye temperature (Θ_D) for $Cd_{1-x}Zn_xTe$ zinc-blende at various compositions x.

		Composition x (%)				
	Method	**0**	**25**	**50**	**75**	**100**
ρ (Kg/m³)	**FP-LAPW LDA**	6025	5920	5905	5880	5680
	FP-LAPW GGA	5445	5440	5385	5390	5150
v_l (m/s)	**FP-LAPW LDA**	3369	3538	3874	3891	4077
	FP-LAPW GGA	3454	3669	3945	3962	4128
	Others	3297 [12]		3726 [12]		3900 [12]
v_t (m/s)	**FP-LAPW LDA**	1612	1819	2015	2026	2154
	FP-LAPW GGA	1631	1886	2035	2048	2246
	Others	1586 [12]		1952 [12]		2114 [12]
v_m (m/s)	**FP-LAPW LDA**	1797	2009	2217	2230	2368
	FP-LAPW GGA	1820	2080	2238	2254	2459
	Others	1783 [12]		2183 [12]		2359 [12]
Θ_D(K)	**FP-LAPW LDA**	167	189	211	212	227
	FP-LAPW GGA	163	185	204	206	226
	Others	165 [12]		212 [12]		235 [12]

The longitudinal sound velocity v_l, which depends primarily on the bulk modulus and shear modulus through the relation:

$$v_l = \sqrt{\frac{B + \frac{4}{3}G}{\rho}}, \tag{12}$$

where ρ denotes the mass density. For each composition, the density is calculated using the standard crystallographic relation:

$$\rho = \frac{NM}{N_A a^3}, \tag{13}$$

In this expression, N is the number of formula units per unit cell, M is the molar mass of the composition, N_A is Avogadro constant (6.022×10^{23} mol^{-1}) and a is the optimized lattice constants listed in Table 2.

As observed in Fig. 7a, the longitudinal sound velocity, which characterizes the propagation speed of compressional waves, exhibits a gradual increase with Zn content. Values rise from approximately 3369–3454 m/s for CdTe to 4077–4128 m/s for ZnTe, this continuous enhancement reflects the gradual hardening of the lattice as Cd atoms are replaced by smaller Zn atoms, forming shorter and tighter Zn–Te bonds. Consequently, the resistance to volumetric deformation increases, leading to higher propagation velocities of longitudinal elastic waves. This behavior is consistent with the compositional evolution of the elastic constants and density, confirming the robustness of the calculated acoustic parameters. As expected, LDA slightly overestimates the velocities compared to GGA, due to its tendency to predict smaller lattice constants and higher elastic stiffness.

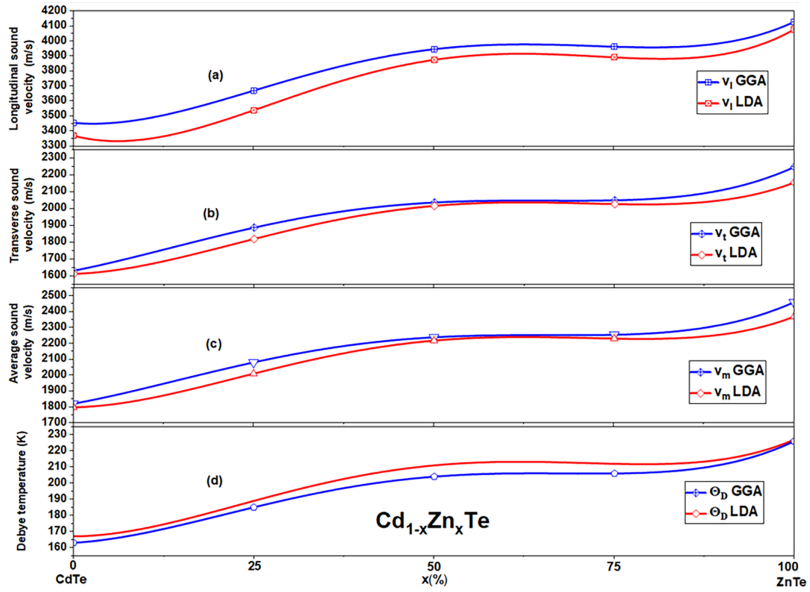

Figure 7: Acoustic and thermal properties of $Cd_{1-x}Zn_xTe$ as a function of Zn concentration: (**a**) Longitudinal sound velocity v_l; (**b**) Transverse sound velocity v_t; (**c**) Average sound velocity v_m; (**d**) Debye temperature Θ_D.

The transverse sound velocity v_t, expressed as:

$$v_t = \sqrt{\frac{G}{\rho}}, \tag{14}$$

As evident in Fig. 7b, the transverse sound velocity, which governs shear wave propagation and is directly related to the shear modulus (G), increases monotonically with Zn concentration. Values range from approximately 1612–1631 m/s for CdTe to 2154–2246 m/s for ZnTe. This behavior reflects the progressive enhancement of resistance to shape deformation, due to the strengthening of directional covalent bonds with increasing Zn content. The compositional dependence of v_t closely mirrors that of the shear modulus. GGA predicts slightly higher transverse velocities than LDA at most compositions, although this tendency

is not strictly uniform across the entire compositional range. The observed deviations remain small and composition-dependent, reflecting subtle differences in equilibrium volume and the treatment of exchange–correlation effects in the two approximations. Overall, both functionals provide a consistent and comparable description of shear wave propagation.

The average sound velocity v_m, often used in estimating Debye temperature, is derived from these components and represents a mean elastic wave speed across all propagation directions [78]. It was calculated using the relation:

$$v_m = \left[\frac{1}{3}\left(\frac{1}{v_l^3} + \frac{2}{v_t^3}\right)\right]^{-\frac{1}{3}}, \tag{15}$$

As illustrated in Fig. 7c, the average sound velocity, derived from the longitudinal and transverse components and used in Debye temperature calculations, shows a steady increase with Zn content. Values rise from approximately 1797–1820 m/s for CdTe to 2368–2459 m/s for ZnTe. This response reflects a continuous, composition-dependent variation in lattice cohesion and elastic wave propagation with increasing Zn content. The average sound velocity, which incorporates both longitudinal and transverse elastic responses, serves as a reliable descriptor of the overall dynamic mechanical behavior of the system. Differences between LDA and GGA predictions are minor and do not alter the monotonic trend, confirming the robustness of the elastic-derived acoustic properties and the reliability of the compositional evolution.

3.5 Thermal Properties

The Debye temperature (Θ_D) is a fundamental thermal parameter governing lattice vibrational dynamics, encapsulating the interplay between interatomic bonding, atomic mass distribution and phonon dispersion. In this work, Θ_D was rigorously derived from the average sound velocity using the Debye continuum model proposed by Anderson [79]. The calculated values for different Zn concentrations are summarized in Table 5 and were obtained from the expression:

$$\Theta_D = \frac{\hbar}{k_B}\left(\frac{3n\rho N_A}{4\pi M}\right)^{\frac{1}{3}} v_m, \tag{16}$$

where $\hbar$ is Planck constant, k_B is Boltzmann constant, n is the number of atoms per formula unit, ρ is the mass density, N_A is Avogadro number and M is the molecular weight. This formulation directly links the macroscopic elastic response to the microscopic thermal properties, providing insight into the progressive stiffening of interatomic bonds with Zn substitution in the CZT lattice.

As shown in Fig. 7d, the Debye temperature increases from 163–167 K for CdTe to 226–227 K for ZnTe, indicating a progressive stiffening of the lattice due to the replacement of weaker Cd–Te bonds with stronger Zn–Te bonds. This reinforcement enhances the force constants of the crystal, leading to higher phonon frequencies and reduced amplitude of lattice vibrations. As a result, phonon activity at operating temperatures becomes less effective in disturbing charge transport, which directly implies a reduction in electron–phonon scattering and thermally activated carrier fluctuations responsible for leakage current and electronic noise. In this sense, the higher Debye temperature indicates a more rigid lattice that is less susceptible to thermally induced distortions affecting charge carriers. Therefore, Zn incorporation mitigates thermally activated noise in CdTe not only by strengthening Zn–Te bonding but also by suppressing lattice vibrations that couple with carriers, thereby improving transport stability compared to pure CdTe. Although LDA slightly overestimates ΘD due to lattice overbinding and enhanced elastic stiffness, while

GGA provides slightly lower values, both approaches consistently confirm the same mechanism, Zn–Te bond reinforcement enhances lattice rigidity, increases Debye temperature, and consequently reduces phonon-mediated scattering processes relevant for room-temperature detector operation.

4 Conclusion

In this work, a systematic first-principles investigation has been conducted to elucidate the composition-dependent mechanical, acoustic and thermal behavior of $Cd_{1-x}Zn_xTe$ alloys across the full concentration range. The results demonstrate that Zn incorporation induces a consistent enhancement of lattice stiffness, as reflected by the increase in elastic moduli, sound velocities and Debye temperature. This behavior is primarily attributed to the progressive formation of stronger and more directional Zn–Te bonds, which reinforce the overall lattice cohesion. Despite this significant increase in rigidity, all studied compositions preserve a ductile mechanical character, as confirmed by Pugh criterion and positive Cauchy pressure values. This coexistence of enhanced stiffness and retained ductility represents a favorable combination rarely observed in compound semiconductors, highlighting the mechanical reliability of the CZT system. Furthermore, the moderate elastic anisotropy and improved resistance to deformation suggest that these alloys can maintain structural integrity under varying mechanical conditions. From an application perspective, the simultaneous improvement in mechanical strength, elastic wave propagation, and thermal stability underscores the suitability of $Cd_{1-x}Zn_xTe$ alloys for advanced technological applications, particularly in radiation detection and optoelectronic devices operating under demanding environments. Overall, this study provides a coherent and predictive framework that can guide the rational design and optimization of CZT-based materials through compositional engineering.

Acknowledgement: The authors would like to acknowledge the computational resources and technical support provided by their respective institutions, which made this work possible.

Funding Statement: The authors received no specific funding for this study.

Author Contributions: The authors confirm contribution to the paper as follows: Conceptualization, Samir Dahmane, Mohammed and Hadj Meliani methodology; Ismail Ouadha; software, Mohammed Traiche; validation, Noureddine Bouteldja; formal analysis, Mohammed Hadj Meliani and Mohamed Belabbas; investigation, Samir Dahmane; resources, Ismail Ouadha and Mohammed Traiche; data curation, Samir Dahmane and Mohamed Belabbas; writing—original draft preparation, Samir Dahmane; writing—review and editing, Mohammed Hadj Meliani, Mohamed Belabbas and Noureddine Bouteldja; visualization, Mohammed Traiche and Ismail Ouadha; supervision, Mohammed Hadj Meliani and Mohamed Belabbas; project administration, Samir Dahmane and Noureddine Bouteldja. All authors reviewed and approved the final version of the manuscript.

Availability of Data and Materials: Not applicable.

Ethics Approval: Not applicable.

Conflicts of Interest: The authors declare no conflicts of interest. The authors confirm that there are no personal, financial or professional relationships that could be construed as influencing the results or interpretation of this study.

References

1. Kuddus A, Mostaque SK, Mouri S, Hossain J. Emerging II–VI wide bandgap semiconductor device technologies. Phys Scr. 2024;99(2):022001. doi:10.1088/1402-4896/ad1858.
2. Tomashyk V, Feychuk P, Shcherbak L. Ternary alloys based on II–VI semiconductor compounds. 1st ed. Boca Raton, FL, USA: CRC Press; 2013. 560 p.

3. Al-Douri Y, Khan MM, Jennings JR. Synthesis and optical properties of II–VI semiconductor quantum dots: a review. J Mater Sci Mater Electron. 2023;34(11):993. doi:10.1007/s10854-023-10435-5.
4. Ravindiran M, Praveenkumar C. Status review and the future prospects of CZTS based solar cell–A novel approach on the device structure and material modeling for CZTS based photovoltaic device. Renew Sustain Energy Rev. 2018;94:317–29. doi:10.1016/j.rser.2018.06.008.
5. Shkir M, Khan MT, Ashraf IM, Almohammedi A, Dieguez E, AlFaify S. High-performance visible light photodetectors based on inorganic CZT and InCZT single crystals. Sci Rep. 2019;9(1):12436. doi:10.1038/s41598-019-48621-3.
6. Surabhi S, Anurag K, Kumar SR. Non-aqueous solution processed CdZnTe thin film via chemical bath deposition: effect of Zn doping variation. Indian J Pure Appl Phys. 2023;61(8):1–8. doi:10.56042/ijpap.v61i8.326.
7. Yoo S, Avendano J, Delmar L, Nam S, Quevedo-Lopez M, Choi H. Band-gap engineering of $Cd_{1-x}Zn_xTe$ films deposited by pulsed laser deposition. Thin Solid Films. 2016;612(185):91–5. doi:10.1016/j.tsf.2016.05.051.
8. Hendi A, Alkhraif R, Alshehri H, AlKallas F, Almoneef M, Laref A, et al. Photovoltaic performance of thin-film CdTe for solar cell applications. J Nanofluids. 2021;10(1):91–7. doi:10.1166/jon.2021.1763.
9. Wolden CA, Abbas A, Li J, Diercks DR, Meysing DM, Ohno TR, et al. The roles of ZnTe buffer layers on CdTe solar cell performance. Sol Energy Mater Sol Cells. 2016;147:203–10. doi:10.1016/j.solmat.2015.12.019.
10. Kadim AM, Shareef AM. Charge carrier mechanism in CdTe/ZnTe core/shell nanocrystals for photoelectrodes by laser ablation method. Al Nahrain J Sci. 2025;28(4):165–72. doi:10.22401/anjs.28.4.13.
11. Schenk M, Hähnert I, Duong LTH, Niebsch HH. Validity of the lattice-parameter vegard-rule in $Cd_{1-x}Zn_xTe$ solid solutions. Cryst Res Technol. 1996;31(5):665–72. doi:10.1002/crat.2170310524.
12. Saib S, Benyettou S, Bouarissa N. *Ab initio* calculation of fundamental properties of $Cd_xZn_{1-x}Te$ ternary alloys in the zinc-blende structure. Phys E Low Dimension Syst Nanostruct. 2015;68:184–9. doi:10.1016/j.physe.2014.12.014.
13. Jiang J. Preparation and performance of CdZnTe ray detector. Mod Electron Technol. 2022;6(1):1. doi:10.26549/met.v6i1.9507.
14. Li Z, Cheng J, Liu F, Wang Q, Wen WW, Huang G, et al. Research on the technological progress of CZT array detectors. Sensors. 2024;24(3):725. doi:10.3390/s24030725.
15. Siltzovalis G, Lagaki V, Madesis I, Mertzimekis TJ. Characterization of a novel, large volume CdZnTe detector for marine applications. Appl Radiat Isot. 2025;226(3):112206. doi:10.1016/j.apradiso.2025.112206.
16. Bouchareb Y, AlSaadi A, Zabah J, Jain A, Al-Jabri A, Phiri P, et al. Technological advances in SPECT and SPECT/CT imaging. Diagnostics. 2024;14(13):1431. doi:10.3390/diagnostics14131431.
17. Szeles C. CdZnTe and CdTe materials for X-ray and gamma ray radiation detector applications. Phys Status Solidi B. 2004;241(3):783–90. doi:10.1002/pssb.200304296.
18. Elmourabit F, Dlimi S, Ouissaaden FI, Khoukh A, Amiri L, Nkhaili L, et al. Structural and optical properties of smooth radio frequency sputtered XTe (X=Cd, Zn) thin films. Phys B Condens Matter. 2023;666(5):415058. doi:10.1016/j.physb.2023.415058.
19. Wei SH, Zhang SB, Zunger A. First-principles calculation of band offsets, optical bowings, and defects in CdS, CdSe, CdTe, and their alloys. J Appl Phys. 2000;87(3):1304–11. doi:10.1063/1.372014.
20. Sher A, Chen AB, Spicer WE, Shih CK. Effects influencing the structural integrity of semiconductors and their alloys. J Vac Sci Technol A Vac Surf Films. 1985;3(1):105–11. doi:10.1116/1.573177.
21. Alowa F, Matsubara M, Schaake C, Bellotti E. Effect of atomic configuration and biaxial strain on the electronic properties of Cd_xZn_{1-x} and $Hg_{1-x}Cd_xTe$ alloys: a first principles study. J Phys D Appl Phys. 2025;58(13):135120. doi:10.1088/1361-6463/adb2a0.
22. Barone V, Ellingson RJ, Khare SV. Bandgap tuning in $ZnxCd_{1-x}Te$ superlattices through variable atomic ordering. J Chem Phys. 2024;161(6):064703. doi:10.1063/5.0221674.
23. Dumre BB, Ellingson RJ, Khare SV. Effects of short-range order on phase equilibria and opto-electronic properties of ternary alloy $Zn_xCd_{1-x}Te$. Sol Energy Mater Sol Cells. 2022;248(1):111971. doi:10.1016/j.solmat.2022.111971.
24. Sharma R, Chuhadiya S, Kamlesh H, Dhaka MS. CdZnTe thin films as proficient absorber layer candidates in solar cell devices: a review. Energy Adv. 2023;2(12):1980–2005. doi:10.1039/d3ya00120b.

25. Beker IM, Dejene FB, Koao LF, Terblans JJ, Werta SZ. Effect of annealing temperature on the structural, optical, and morphological properties of CdZnTe thin films produced by a simple two-electrode electrodeposition system for solar cell application. ECS J Solid State Sci Technol. 2025;14(6):064004. doi:10.1149/2162-8777/ade3a0.
26. Tedjini MH, Oukebdane A, Belkaid MN, Aouail N. The effect of zinc concentration upon electronic structure, optical and dielectric properties of $Cd_{1-x}Zn_xTe$ alloy: TB-mBJ investigation. Comput Condens Matter. 2021;27(3):e00561. doi:10.1016/j.cocom.2021.e00561.
27. Wan X, Cao K, Li Y, Wei H, Jiang R, Liu Y, et al. Preparation and characterization of large-sized CdZnTe epitaxial single crystal. Nucl Instrum Meth Phys Res Sect A Accel Spectrometers Detect Assoc Equip. 2023;1056:168625. doi:10.1016/j.nima.2023.168625.
28. Park C, Kim S, Kim H, Jeong WY, Park H, Yeom JY, et al. Preliminary study of CdZnTe for multipurpose radiation detection in broadband applications. Radiat Meas. 2025;186(5):107457. doi:10.1016/j.radmeas.2025.107457.
29. Zhang SB, Wei SH. Self-doping of cadmium stannate in the inverse spinel structure. Appl Phys Lett. 2002;80(8):1376–8. doi:10.1063/1.1452789.
30. Liu Y, Liu BG. Ferromagnetism in transition-metal-doped II–VI compounds. J Magn Magn Mater. 2006;307(2):245–9. doi:10.1016/j.jmmm.2006.04.009.
31. Alhaddad T, Shoker MB, Pagès O, Postnikov AV, Torres VJB, Polian A, et al. Raman study of $Cd_{1-x}Zn_xTe$ phonons and phonon-polaritons—experiment and *ab initio* calculations. J Appl Phys. 2023;133(6):065701. doi:10.1063/5.0134454.
32. Man MT, Lee HS. Influence of temperature and excitation density on carrier dynamics in CdZnTe quantum dots. Sci Rep. 2025;15(1):21454. doi:10.1038/s41598-025-07292-z.
33. Man MT, Lee HS. Discrete states and carrier-phonon scattering in quantum dot population dynamics. Sci Rep. 2015;5(1):8267. doi:10.1038/srep08267.
34. Szeles C. Advances in the crystal growth and device fabrication technology of CdZnTe room temperature radiation detectors. IEEE Trans Nucl Sci. 2004;51(3):1242–9. doi:10.1109/TNS.2004.829391.
35. Li X, Jiang X, Xiang Y, Huang X, Li X, Wei L, et al. Study on energy resolution improvement of pixelated CdZnTe detectors based on 3D position sensitivity. J Instrum. 2025;20:P07043. doi:10.1088/1748-0221/20/07/P07043.
36. Ke SH, Baranger HU, Yang W. Role of the exchange-correlation potential in *ab initio* electron transport calculations. J Chem Phys. 2007;126(20):201102. doi:10.1063/1.2743004.
37. Evans JS, Vydrov OA, Van Voorhis T. Exchange and correlation in molecular wire conductance: nonlocality is the key. J Chem Phys. 2009;131(3):034106. doi:10.1063/1.3179754.
38. van de Walle A, Ceder G. Correcting overbinding in local-density-approximation calculations. Phys Rev B. 1999;59(23):14992–5001. doi:10.1103/physrevb.59.14992.
39. Perdew JP, Chevary JA, Vosko SH, Jackson KA, Pederson MR, Singh DJ, et al. Atoms, molecules, solids, and surfaces: applications of the generalized gradient approximation for exchange and correlation. Phys Rev B. 1992;46(11):6671–87. doi:10.1103/physrevb.46.6671.
40. Wu Z, Cohen RE. More accurate generalized gradient approximation for solids. Phys Rev B. 2006;73(23):235116. doi:10.1103/physrevb.73.235116.
41. Hohenberg P, Kohn W. Inhomogeneous electron gas. Phys Rev. 1964;136(3B):B864–71. doi:10.1103/physrev.136.b864.
42. Kohn W, Sham LJ. Self-consistent equations including exchange and correlation effects. Phys Rev. 1965;140(4A):A1133–8. doi:10.1103/physrev.140.a1133.
43. Blaha P. *WIEN*2k: an augmented plane wave plus local orbital package for the electronic structure of solids. In: International tables for crystallography. Chester, UK: International Union of Crystallography; 2021. p. 836–42. doi:10.1107/s1574870720003171.
44. Schwarz K, Blaha P, Madsen GKH. Electronic structure calculations of solids using the WIEN2k package for material sciences. Comput Phys Commun. 2002;147(1–2):71–6. doi:10.1016/S0010-4655(02)00206-0.
45. Schwarz K, Blaha P. Solid state calculations using WIEN2k. Comput Mater Sci. 2003;28(2):259–73. doi:10.1016/S0927-0256(03)00112-5.

46. Perdew JP, Zunger A. Self-interaction correction to density-functional approximations for many-electron systems. Phys Rev B. 1981;23(10):5048–79. doi:10.1103/physrevb.23.5048.
47. Perdew J, Burke K, Ernzerhof M. Generalized gradient approximation made simple. Phys Rev Lett. 1996;77(18):3865–8. doi:10.1103/PhysRevLett.77.3865.
48. Jamal M, Reshak AH. One- and two-dimensional search of an equation of state using a newly released 2DRoptimize package. J Phys Chem Solids. 2018;116(1):131–6. doi:10.1016/j.jpcs.2018.01.034.
49. Murnaghan FD. The compressibility of media under extreme pressures. Proc Natl Acad Sci U S A. 1944;30(9):244–7. doi:10.1073/pnas.30.9.244.
50. Song WB, Yu MY, Wu WH. Crystal growth and characterization of CdTe from the melt under controlled Cd partial pressure. J Cryst Growth. 1988;86(1–4):127–31. doi:10.1016/0022-0248(90)90709-T.
51. Jin M, He F, Zheng S, Xu Y, Peng Y, Chen X, et al. Growth of ZnTe semiconductor crystal via a Te flux zone melting method and characterization of its properties. Cryst Res Technol. 2022;57(10):2100279. doi:10.1002/crat.202100279.
52. Duan H, Chen X, Huang Y, Zhou X, Sun L, Lu W. Composition-dependent electronic properties, optical transitions, and anionic relaxations of $Cd_{1-x}Zn_xTe$ alloys from first principles. Phys Rev B. 2007;76(3):035209. doi:10.1103/physrevb.76.035209.
53. Bouarissa N, Atik Y. Elastic constants and acoustic wave velocities IN$Cd_{1-x}Zn_x$TeMIXED crystals. Mod Phys Lett B. 2008;22(12):1221–9. doi:10.1142/s0217984908015371.
54. Konovalenko OI. Study of phase equilibrium of zinc-tellur compounds for improvement of properties of functional material radiation sensors. Collect Sci Works Mil Inst Kyiv Natl Taras Shevchenko Univ. 2021;(72):20–4. doi:10.17721/2519-481x/2021/72-03.
55. Cantor B. Hooke's law: elasticity. In: The equations of materials. Oxford, UK: Oxford University Press; 2020. p. 207–25. doi:10.1093/oso/9780198851875.003.0010.
56. Jamal M. A package for calculating elastic tensors of cubic phases by using second-order derivative with WIEN2k Package. User's Guide, Cubic-elastic_13.2 (Release 27.08.2013) [Internet]; 2013 [cited 2026 Jan 1]. Available from: https://fr.scribd.com/document/420738822/Guide-Cubic-1.
57. McSkimin HJ, Thomas DG. Elastic moduli of cadmium telluride. J Appl Phys. 1962;33(1):56–9. doi:10.1063/1.1728527.
58. Yamada M, Yamamoto K, Abe K. Elastic and photoelastic constants of ZnTe measured by Brillouin scattering. J Phys D Appl Phys. 1977;10(10):1309–13. doi:10.1088/0022-3727/10/10/006.
59. Korozlu N, Colakoglu K, Deligoz E. Structural, electronic, elastic and optical properties of $Cd_xZn_{1-x}Te$ mixed crystals. J Phys Condens Matter. 2009;21(17):175406. doi:10.1088/0953-8984/21/17/175406.
60. Khenata R, Bouhemadou A, Sahnoun M, Reshak AH, Baltache H, Rabah M. Elastic, electronic and optical properties of ZnS, ZnSe and ZnTe under pressure. Comput Mater Sci. 2006;38(1):29–38. doi:10.1016/j.commatsci.2006.01.013.
61. Wang J, Yip S, Phillpot SR, Wolf D. Atomic-scale simulations of mechanical properties. Phys Rev Lett. 1993;71(24):4182–5. doi:10.1103/PhysRevLett.71.4182.
62. Man CS, Huang M. A simple explicit formula for the Voigt-Reuss-hill average of elastic polycrystals with arbitrary crystal and texture symmetries. J Elast. 2011;105(1):29–48. doi:10.1007/s10659-011-9312-y.
63. Bhagavantam S, Rao TS. Compressibilities of cubic crystalline powders: a new method of measurement. Nature. 1951;168(4278):744. doi:10.1038/168744a0.
64. Merad AE, Kanoun MB, Aourag H, Cibert J, Merad G. Electronic and optical properties of CdTe under hydrostatic pressure effect. Superlattices Microstruct. 2002;32(1):25–34. doi:10.1006/spmi.2002.1054.
65. Kishore N, Nagarajan V, Chandiramouli R. Mechanical properties and band structure of CdSe and CdTe nanostructures at high pressure—a first-principles study. Process Appl Ceram. 2019;13(2):124–31. doi:10.2298/pac1902124k.
66. Deligoz E, Colakoglu K, Ciftci Y. Elastic, electronic, and lattice dynamical properties of CdS, CdSe, and CdTe. Phys B Condens Matter. 2006;373(1):124–30. doi:10.1016/j.physb.2005.11.099.

67. Lalitha S, Karazhanov SZ, Ravindran P, Senthilarasu S, Sathyamoorthy R, Janabergenov J. Electronic structure, structural and optical properties of thermally evaporated CdTe thin films. Phys B Condens Matter. 2007;387(1–2):227–38. doi:10.1016/j.physb.2006.04.008.
68. Bilal M, Shafiq M, Ahmad I, Khan I. First principle studies of structural, elastic, electronic and optical properties of Zn-chalcogenides under pressure. J Semicond. 2014;35(7):072001. doi:10.1088/1674-4926/35/7/072001.
69. Kiran MSRN, Kshirsagar S, Krishna MG, Tewari SP. Structural, optical and nanomechanical properties of (1 1 1) oriented nanocrystalline ZnTe thin films. Eur Phys J Appl Phys. 2010;51(1):10502. doi:10.1051/epjap/2010071.
70. Górecki T. The relations between the shear modulus, the bulk modulus and Young's modulus for polycrystalline metallic elements. Mater Sci Eng. 1980;43(3):225–30. doi:10.1016/0025-5416(80)90106-8.
71. Eberhart ME, Jones TE. Cauchy pressure and the generalized bonding model for nonmagnetic bcc transition metals. Phys Rev B. 2012;86(13):134106. doi:10.1103/physrevb.86.134106.
72. Chen XQ, Niu H, Li D, Li Y. Modeling hardness of polycrystalline materials and bulk metallic glasses. Intermetallics. 2011;19(9):1275–81. doi:10.1016/j.intermet.2011.03.026.
73. Senkov ON, Miracle DB. Generalization of intrinsic ductile-to-brittle criteria by Pugh and Pettifor for materials with a cubic crystal structure. Sci Rep. 2021;11(1):4531. doi:10.1038/s41598-021-83953-z.
74. Thompson RP, Clegg WJ. Predicting whether a material is ductile or brittle. Curr Opin Solid State Mater Sci. 2018;22(3):100–8. doi:10.1016/j.cossms.2018.04.001.
75. Mott PH, Dorgan JR, Roland CM. The bulk modulus and Poisson's ratio of "incompressible materials". J Sound Vib. 2008;312(4–5):572–5. doi:10.1016/j.jsv.2008.01.026.
76. Ledbetter H, Migliori A. A general elastic-anisotropy measure. J Appl Phys. 2006;100(6):063516. doi:10.1063/1.2338835.
77. Jaeken JW, Cottenier S. Solving the Christoffel equation: phase and group velocities. Comput Phys Commun. 2016;207(4):445–51. doi:10.1016/j.cpc.2016.06.014.
78. Wolfenden A, Harmouche MR. An improved method of using sound velocity measurements to determine the Debye temperature of cubic and noncubic materials. J Appl Phys. 1992;72(7):2732–8. doi:10.1063/1.351523.
79. Anderson OL. A simplified method for calculating the debye temperature from elastic constants. J Phys Chem Solids. 1963;24(7):909–17. doi:10.1016/0022-3697(63)90067-2.